Developmental Biology 527 (2025) 250–259

Contents lists available at ScienceDirect

Developmental Biology

journal homepage: www.elsevier.com/locate/developmentalbiology

Original research article

The PRC2-associated factor EPOP is required for *Hox* gene regulation during axial development in mice

Ivano Mocavini [a,1,2], Anna Mallol [a,1], Arantxa Gutierrez [a], Paul Chammas [a], Ana Carretero [b], André Dias [c], Enrique Blanco [a], Irene Rodriguez Arce [a], Moises Mallo [d], Luciano Di Croce [a,c,e,*], Bernhard Payer [a,c,**,3]

[a] Centre for Genomic Regulation (CRG), The Barcelona Institute for Science and Technology, Carrer del Doctor Aiguader 88, Barcelona, 08003, Spain
[b] Department of Animal Health and Anatomy, School of Veterinary Medicine, Universitat Autònoma de Barcelona, Bellaterra, Spain
[c] Universitat Pompeu Fabra (UPF), Carrer del Doctor Aiguader 88, Barcelona, 08003, Spain
[d] Gulbenkian Institute for Molecular Medicine, Edifício Egas Moniz, Av. Professor Egas Moniz, 1649-028, Lisbon, Portugal
[e] ICREA, Passeig Lluís Companys 23, 08010, Barcelona, Spain

ARTICLE INFO

Keywords:
EPOP
Polycomb
PRC2
Hox genes
Body patterning

ABSTRACT

The Polycomb repressive complex 2 (PRC2) is an essential modulator of gene repression. We previously reported that, in mouse embryonic stem cells, PRC2 associates with elonginB/C through EPOP, which allows for low-level expression of target genes. Here we investigate the role of EPOP *in vivo* by generating a mouse knockout (KO) model. We show that *Epop* KO mice are viable and fertile but display highly penetrant posterior homeotic transformations of the axial skeleton, which can be partially recapitulated by deletion of only the maternal allele. *Epop*-depleted embryos present a shift of the anterior boundary of expression of certain *Hox* genes. Tissue-specific RNA sequencing of embryos suggests that the *Hox* activation defect originates at the level of the presomitic mesoderm. Overall, we find that EPOP prevents premature activation of a subset of *Hox* genes, and that this is required for correct body patterning along the antero-posterior axis.

1. Introduction

The Polycomb group (PcG) of genes mediates maintenance of the epigenetic memory of gene silencing (Kim and Kingston, 2022; Schuettengruber et al., 2017). PcG protein products assemble into two main macromolecular complexes, the Polycomb repressive complex 1 (PRC1) and PRC2. Both complexes mark silenced chromatin loci with specific histone post-translational modifications (PTMs): mono-ubiquitination of histone H2A at lysine 119 (H2AK119ub) by PRC1, and mono-, di-, and tri-methylation of histone H3 at lysine 27 (H3K27me1/2/3) by PRC2.

Establishing an appropriate H3K27 methylation pattern is necessary for numerous biological processes during the developmental trajectory of the organism, including cell lineage commitment, genomic imprinting, X-chromosome dosage compensation, and patterning of the antero-posterior (A-P) axis (Condemi et al., 2025; Gentile and Kmita, 2020; Inoue, 2023; Loda et al., 2022). This latter process is regulated by the expression of the *Hox* gene family, which comprises 39 highly conserved genes in mammals that encode for homeodomain transcription factors. *Hox* genes are organized into four clusters (*HoxA*, *HoxB*, *HoxC*, and *HoxD*) that are sequentially triggered in time and space during embryonic development (Deschamps and Duboule, 2017; Deschamps and van Nes, 2005). Mutations of several *Hox* genes and/or entire paralogous groups result in changes in the anatomical features of

* Corresponding author. Centre for Genomic Regulation (CRG), The Barcelona Institute for Science and Technology, Carrer del Doctor Aiguader 88, Barcelona 08003, Spain.
** Corresponding author. Centre for Genomic Regulation (CRG), The Barcelona Institute for Science and Technology, Carrer del Doctor Aiguader 88, Barcelona 08003, Spain.
E-mail addresses: Luciano.DiCroce@crg.eu (L. Di Croce), bernhard.payer@umontreal.ca (B. Payer).
[1] These authors contributed equally to this work.
[2] Present address: Department of Biochemistry and Molecular Biotechnology, University of Massachusetts Chan Medical School, Worcester, MA 01605, USA.
[3] Present address: Department of Pathology and Cellular Biology, University of Montreal and Azrieli Research Centre of CHU Sainte-Justine, 3175 Cote Sainte-Catherine, Montreal, Quebec, H3T 1C5, Canada.

https://doi.org/10.1016/j.ydbio.2025.08.014
Received 11 April 2025; Received in revised form 14 August 2025; Accepted 17 August 2025
Available online 18 August 2025

specific vertebrae, creating vertebrae that in most cases resemble more anterior ones (Horan et al., 1995; McIntyre et al., 2007; Wellik and Capecchi, 2003), a phenotype known as anterior homeotic transformation. Thus, expression of these genes is critical for the correct morphogenesis of embryonic axial structures (Deschamps and Duboule, 2017; Deschamps and van Nes, 2005; Mallo et al., 2010). During somitogenesis, progressive activation of the *Hox* gene clusters is counteracted by the actions of PcG factors, through the dynamic deposition of H3K27me3 (Neijts et al., 2016; Soshnikova and Duboule, 2009), which can result in posterior homeotic transformation if altered (Akasaka et al., 1996; Isono et al., 2005; Lau et al., 2017; Takihara et al., 1997; van der Lugt et al., 1994; Vizán et al., 2020; Wang et al., 2007).

The roles of the elonginBC and the PRC2-associated protein EPOP in mESCs has been previously characterized. Specifically, EPOP assembles into a PRC2 complex devoid of JARID2 and AEBP2, and modulates transcription both at H3K27me3-marked genomic sites and at active broad H3K4me3 domains in mESC chromatin (Beringer et al., 2016; Liefke et al., 2016). Moreover, a PRC2 complex that includes EPOP and the short splicing isoform of SUZ12 (SUZ12-S) has higher dimerization propensity resulting in H3K27 hypermethylation at target promoters (Arecco et al., 2024).

Here, we investigate the role of EPOP *in vivo*. We find that *Epop* knockout (KO) mice are viable and fertile, with no major defects in several of the PRC2-related developmental processes. However, mice with a full KO or with a maternal null allele produce offspring with posterior homeotic transformations. The phenotype is accompanied by *Hox* gene misexpression at an early stage during somitogenesis. Overall, our data suggest that maternal EPOP provision is necessary for correct skeletal patterning through its regulation of timely *Hox* gene activation.

2. Results

2.1. Generation of Epop knockout mice

As EPOP is expressed during early mouse development (Beringer et al., 2016), we analyzed its function during embryogenesis by generating *Epop* KO mice. We first tested the *in vitro* editing efficiency of three different sgRNAs targeting the coding sequence of *Epop* (Epop-KO1–3, Fig. S1A–C). Using the embryos treated with the most efficient sgRNA (Epop-KO1) and the Cas9 protein, we transferred 16 injected embryos to pseudopregnant females, resulting in the birth of seven potential founder mice (Fig. S1D).

Of the various mutant alleles generated, mice with deletions of 13 or 14 nucleotides in the *Epop* gene (del13 and del14, respectively), as detected by standard agarose gels, were selected as potential colony founders. Germline transmission of these mutant alleles was confirmed by breeding the mice to wild-type C57Bl/6 mice, and the resulting $Epop^{+/-}$ pups were selected to establish new transgenic colonies. Sequencing the del13 and del14 alleles revealed a frameshift that gave rise to short mutant proteins (83 and 159 amino acids (aa), respectively), which shared only the first 28 or 29 aa of the 370-aa EPOP protein (Fig. 1A). Genotyping of the F1 offspring showed the expected Mendelian and sex ratios (Fig. 1A–C, Fig. S1E) and no significant differences in the number or size of the litters (Fig. 1D). No EPOP protein was present and no gross overall changes in SUZ12 or H3K27me3 levels were detected in head and placenta samples of E12.5 *Epop* KO embryos by Western blot (Fig. 1E, Fig. S1F). In conclusion, our CRISPR-generated *Epop* KO mice are devoid of EPOP protein, are viable, and breed normally.

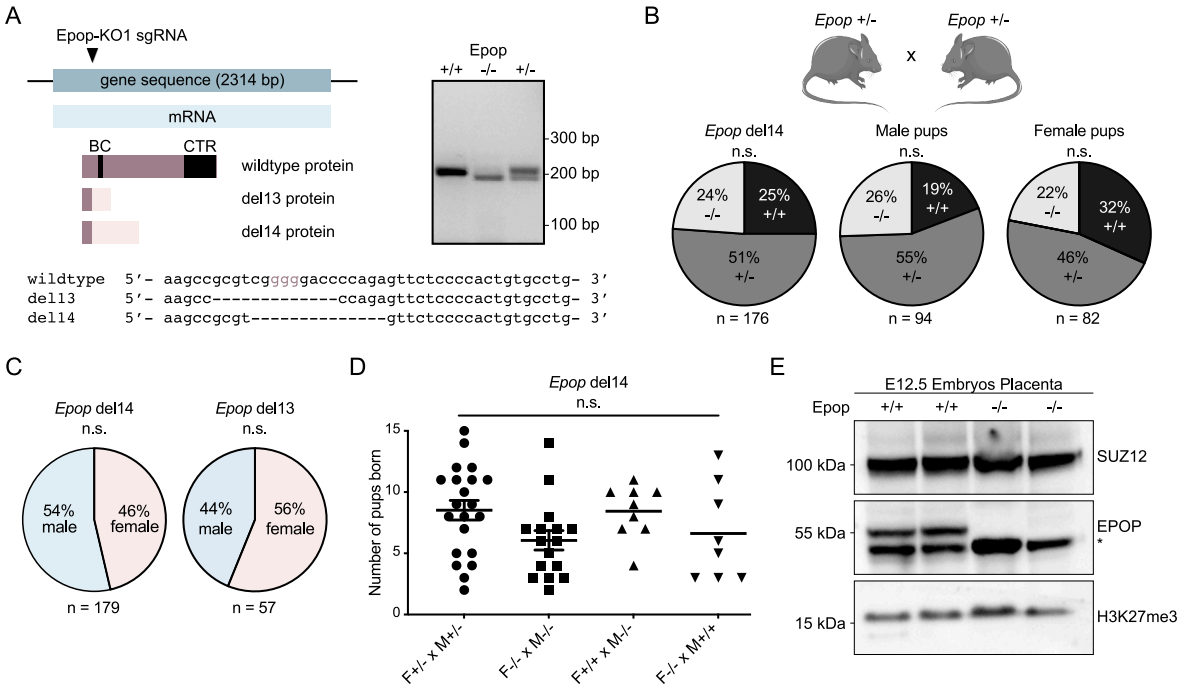

Fig. 1. Generation of *Epop* knockout mice using the CRISPR/Cas9 system. (A) Gene targeting strategy for the *Epop* allele. Two mutated alleles with deletions of 13 (del13) or 14 (del14) nucleotides were selected (PAM indicated in brown). A representative gel image of the genotyping PCR using the Epop-10 primers is shown. BC, elongin B/C binding box; CTR, C-terminal region binding SUZ12. **(B,C)** Mendelian (B) and sex (C) ratios after heterozygous matings were calculated. Chi-square and Binomial tests were used for statistical analysis, respectively. **(D)** Litter size from different $Epop^{+/-}$ crossings. The Kruskal–Wallis test was used to compare litter size among matings. **(E)** Detection of SUZ12, EPOP, and H3K27me3 via Western blot from placenta extracts from E12.5 embryos (*Epop* −/−, del14 strain). The asterisk indicates a non-specific band below the main EPOP band (~55 kDa). (For interpretation of the references to color in this figure legend, the reader is referred to the Web version of this article.)

2.2. EPOP-depleted blastocysts show normal cell lineage segregation and X-chromosome reactivation

Our analysis of data from the Vertebrate Alternative Splicing and Transcription Database (VastDB) (Tapial et al., 2017) revealed that *Epop* is highly expressed only at the blastocyst stage during mouse preimplantation embryo development (Fig. S2A). We confirmed the presence of EPOP in the inner cell mass (ICM) of mouse blastocysts (Beringer et al., 2016) by immunofluorescence (Fig. 2A). Using single-cell RNA expression data (Mohammed et al., 2017; Pijuan-Sala et al., 2019), we found that *Epop* RNA at later developmental stages was downregulated upon gastrulation (Fig. 2B) and thereafter was expressed in various embryonic tissues, including the neural crest, the paraxial and caudal mesoderm, and the extraembryonic endoderm (Fig. S2B).

Given its specific expression in the ICM and its role in mESCs (Beringer et al., 2016), we next assessed cell lineage segregation in *Epop* KO mice by collecting *in vivo* fertilized embryos from a heterozygous mating (*Epop* del14) at E3.5 and culturing them *in vitro* for 24 h to obtain

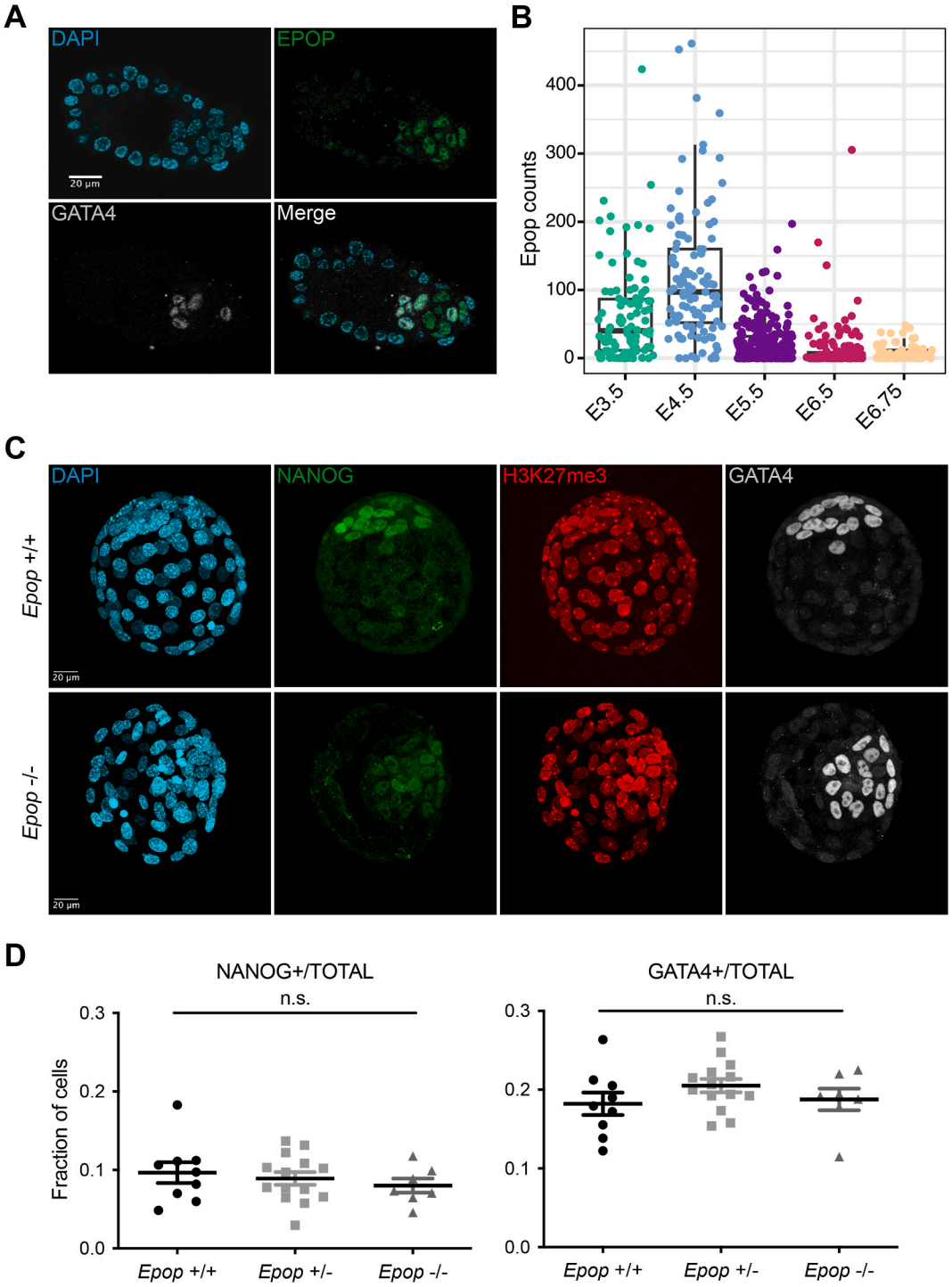

Fig. 2. *Epop* is not necessary for inner cell mass sorting into epiblast and primitive endoderm. (A) Staining of EPOP and GATA4 in the early mouse blastocyst. **(B)** Expression of *Epop* RNA in mouse gastrulating embryos (single cell RNA-seq data from Mohammed et al., 2017). **(C)** Staining of NANOG, H3K27me3, and GATA4 in E4.5 blastocysts derived from wild-type or *Epop*$^{-/-}$ mice (del14 strain), as indicated at the top. **(D)** Quantification of NANOG and GATA4 positive cells from (C).

late blastocysts. No significant differences in total (DAPI-positive), epiblast (NANOG-positive), or primitive endoderm (GATA4-positive) cell numbers were detected between the three *Epop* genotypes (+/+, +/−, and −/−; Fig. 2C and D). To corroborate our *Epop* KO results by a complementary siRNA knockdown approach, we assessed cell lineage segregation in blastocysts after knocking down *Epop* by injecting two different siRNAs (Epop-KD1 or -KD2) into one-cell embryos. Both groups of embryos reached blastocyst stage at normal rates (Fig. S3A–C). Blastocyst quality was assessed by differential staining of epiblast (NANOG-positive) and primitive endoderm (GATA4-positive) cells. We did not observe changes in the number of cells per blastocyst after knockdown with either Epop-KD siRNA as compared to the control siRNA (Fig. S3D and E). Furthermore, although EPOP is known to modulate PRC2 activity (Beringer et al., 2016) and H3K27me3 is erased from the inactive X chromosome in female blastocyst epiblast cells during X-chromosome reactivation (XCR) (Mak et al., 2004), we observed normal XCR dynamics based on removal of the H3K27me3 spot representing the inactive X in Epop-KD2-injected embryos at 96 h post-injection (around embryonic day [E] 3.5 to E4.5) (Fig. S3E). Moreover, the one female *Epop* −/− embryo in our KO analysis displayed also a loss of the H3K27me3 spots in epiblast cells, suggesting XCR to occur (Fig. 2C). These results, together with the fact that *Epop* KO mice are born at normal rates, suggest that EPOP is dispensable for early cell fate commitment and H3K27me3 erasure from the inactive X chromosome during its reactivation in mouse blastocysts. Further characterization will be needed to exclude potential XCR defects including at the transcriptional reactivation level of X-linked genes.

2.3. *Epop KO mice show highly penetrant homeotic transformations*

To analyze whether *Epop* KO mice display homeotic transformations similarly to null mice for other polycomb-associated factors (Akasaka et al., 1996; Isono et al., 2005; Lau et al., 2017; Takihara et al., 1997; van der Lugt et al., 1994; Vizán et al., 2020; Wang et al., 2007), we analyzed for skeletal variations in adult mice. Indeed, *Epop* KO mice (n = 20) showed a higher penetrance of skeletal variations than wild-type mice (n = 24) (Fig. 3). Specifically, *Epop* KO mice showed: *i*) partial or complete fusion of the atlas and axis (corresponding to cervical vertebrae C1 and C2, respectively); *ii*) a reduced or missing spinous process of the axis in 12 of 16 (del14) or 2 of 4 (del13) KO mice; and *iii*) an ectopic rib in the transverse process of C7, at a penetrance of 90 % in KO mice (15 of the 16 del14, and 3 of the 4 del13), indicating a "T1-like" identity for C7 (Fig. 3A). The shape of the extra rib was variable, presenting either just the head, a partial rib fused to the costal cartilage of the next rib (Y-shape), or a complete rib articulated with the sternum (Fig. 3A). Consequently, only 12 vertebrae were found at the thoracic region of *Epop* KO mice, followed by six lumbar vertebrae and four sacral vertebrae (Fig. 3B and C). T1 showed a transformation into T2 (Fig. 3), characterized by the presence of a spinous process in T1, in 15 of the 16 del14, and 3 of the 4 del13, KO mice (90 % penetrance, Fig. 3A). Finally, T13 showed no ribs, leading to a T13–to–L1 transformation (80 % penetrance, Fig. 3B). A misshapen sternum, in some cases specifically affecting the manubrium or the xiphisternum, was also observed in 8 of the 20 *Epop* KO mice analyzed (with 5 from del14, and 3 from del13; 40 % penetrance). Moreover, the fourth sternebrae was reduced or missing in 8 of the 20 *Epop* KO mice analyzed (40 % penetrance, Fig. S4A). Transformations were observed in both male and female mice (see details in Table S2). Overall, these alterations indicated that the normal skeletal pattern was shifted, giving rise to a highly penetrant posterior transformation of the axial skeleton in *Epop* KO mice (Fig. 3C and Fig. S4). These transformations and their penetrance resembled the null phenotypes of mice deficient in PRC1-associated factors, such as *Cbx2*

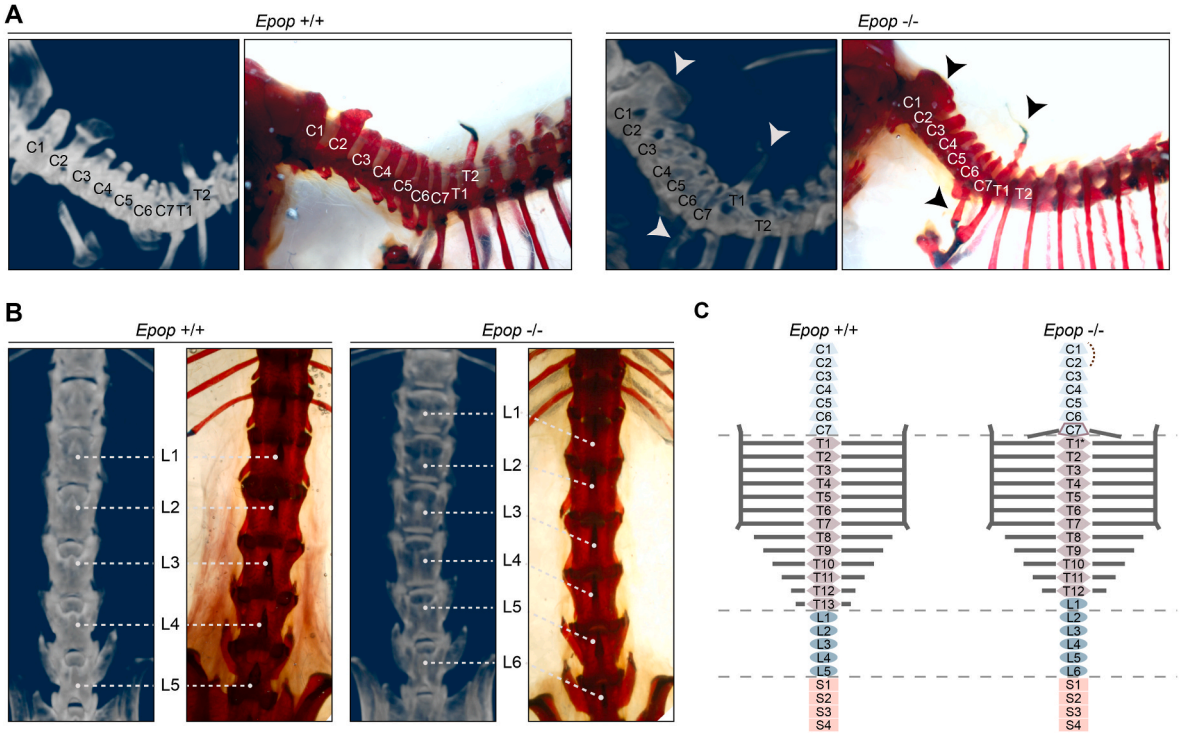

Fig. 3. *Epop* KO mice present highly penetrant posterior homeotic transformations. (A) Lateral vision of cervical vertebrae of micro-CT 3D images (left) or after skeletal whole mount staining (right) of wild-type (+/+, left) and *Epop* KO (−/−, right). The fusion of C1 and C2, an Y-shaped extra rib in C7, and a prominent spinous process in T1 are observed in *Epop* KO mice (arrowheads). **(B)** Dorsal vision of lumbar vertebrae of micro-CT 3D images (left) or after skeletal whole mount staining (right). **(C)** Schematic overview of the axial vertebrae indicated in different colors. Light blue, cervical; purple, thoracic; intense blue, lumbar; and pink, sacral. Gray horizontal lines indicate the thoracic ribs, with T1-T7 forming the sternocostal junctions with the sternum. *Epop* KO mice display a C1–C2 fusion and C7 to T1, T1 to T2, and T13 to L1 transformations, resulting in a pattern of 12 thoracic vertebrae and 6 lumbar vertebrae. (For interpretation of the references to color in this figure legend, the reader is referred to the Web version of this article.)

(Lau et al., 2017), *Phc2* (Isono et al., 2005), and *Pcgf4* (van der Lugt et al., 1994). In contrast, mice null for the PRC2-associated factor *Phf19* show lower penetrance (around 40 %) (Vizán et al., 2020); notably, Phf19 is part of the PRC2.1 complex together with EPOP.

Recent reports show that maternal deletion of the epigenetic regulator *Smchd1* results in a similar posterior homeotic transformation of the skeleton (Benetti et al., 2022; Xue et al., 2022). As this factor is thought to act downstream of Polycomb, we next analyzed whether EPOP also has a parental effect on body patterning. Analysis of heterozygous mice derived from *Epop*$^{-/-}$ mothers (*Epop*$^{mat\Delta}$) revealed a pattern of alterations like the one observed in *Epop* KO mice, albeit with a reduced penetrance (Fig. S4B and Table 1). Conversely, most mice that inherited the null allele from the father (*Epop*$^{pat\Delta}$) displayed a normal skeletal patterning (Table 1). Overall, our results suggest that, similar to SMCHD1 (Benetti et al., 2022; Xue et al., 2022), a maternal EPOP deficiency leads to an abnormal epigenetic state that results in homeotic skeletal transformations during postimplantation development.

2.4. *Hox genes are misexpressed in Epop KO embryos*

Next, we investigated the expression of the *Hox* gene family, which has a key role in the differentiation of the axial skeleton into the different vertebrae (Deschamps and Duboule, 2017). In particular, we performed whole-mount *in situ* hybridization to analyze the expression patterns of: the *Hox6* group, which is involved in rib cage differentiation; the *Hox8* group; and the *Hox10* group, which turns the rib program off during somatic patterning and specification (Carapuço et al., 2005; McIntyre et al., 2007; Wellik and Capecchi, 2003). We found that the anterior boundary of expression of both *Hoxa6* and *Hoxc6* was shifted one somite more rostrally in *Epop* KO mice, with respect to wild-type mice, at E9.0 and E10.5. In contrast, we observed no differences in the expression patterns of *Hoxb8* at E10.5 or of *Hoxc10* at E11.5 (Fig. 4A).

Somites differentiate from the growing presomitic mesoderm (PSM) in the tailbud of the embryo, between approximately E7.5 and E13.5 (Deschamps and Duboule, 2017). During this time, temporal collinear activation of the *Hox* clusters results in the assignment of a Hox transcriptional signature to each new pair of somites generated from the PSM. To determine whether *Hox* misexpression came from precocious activation of the *Hox* clusters in the PSM, we dissected the posterior part of the tailbud of 4- and 5-somite–matched E8.5 embryos and performed RNA-seq, using four wild-type and four KO (Fig. 4B). Differential expression analysis revealed that only 42 genes were differentially expressed ($fdr < 0.05$) in the PSM of *Epop* KO embryos with respect to wild-type (Fig. 4C), with no enrichment for specific gene ontologies (data not shown). However, inspection of the *Hox* gene family revealed upregulation of both *Hoxb8* (2.2-fold, p-value $= 7.1 \times 10^{-8}$) and *Hoxa10* (1.5-fold, p-value $= 7.3 \times 10^{-4}$) (Fig. 4D and E). No significant changes in the *Hox* expression patterns were found between samples from 4- and 5-somite embryos (Fig. S5A). These results suggest that rostral shifts in *Hox* expression boundaries in *Epop* KO mice may result from precocious activation of the *Hox* gene clusters in the PSM during somitogenesis.

3. Discussion

PRC2 is a key epigenetic regulator that mediates gene silencing in a plethora of developmental processes, and alterations of these are associated with various overgrowth syndromes and tumorigenesis (Chammas et al., 2019). In recent years, several labs have described the important roles played by accessory factors in modulating PRC2 activity and its recruitment to chromatin. Here we investigated the role of the Polycomb-associated factor EPOP in mouse development. We find that *Epop* KO mice undergo highly penetrant posterior homeotic transformations due to a rostral shift in the boundary of expression of several *Hox* genes. Mutations of other PRC2 accessory factors, such as *Jarid2*, *Mtf2*, or *Phf19*, produce a pleiotropic phenotype, with defects ranging from growth retardation to neural, cardiac, and blood abnormalities (Rothberg et al., 2018; Takeuchi et al., 1995, 1999; Vizán et al., 2020; Wang et al., 2007). A detailed histopathology of *Epop* KO mice did not reveal any major defects (data not shown), suggesting that a main role of EPOP is to ensure faithful antero-posterior body patterning.

While characterizing the molecular basis of the *Epop* phenotype, we observed that misexpression of specific *Hox* genes in *Epop* KO embryos was already visible in the PSM at E8.5. Notably, two genes that we found to be upregulated (*Hoxb8* and *Hoxa10*) belong precisely to the mid-late *Hox* paralogous group, which transitions towards transcription activation at this time point (Fig. S5A). Hence, we speculate that the absence of *Epop* results in a faster activation of the *Hox* gene clusters in the PSM. This acceleration of the "Hox clock" would translate into an ordered rostral shift of the *Hox* expression pattern – as described here and for many other PcG mutants (Akasaka et al., 1996, 2001; Bel et al., 1998; Isono et al., 2005; Li et al., 2011; Suzuki et al., 2002; Takihara et al., 1997; Wang et al., 2002) – without disrupting their spatial collinearity. This mechanism, although in the opposite direction, could also be at the basis for the anterior transformations observed in Trithorax mutants (Baskind et al., 2009; Fisher et al., 2010; Yu et al., 1995), as well as in some "unconventional" PcG mutants, such as *Aebp2*, *Pcgf6*, and *Ring1a* (del Mar Lorente et al., 2000; Endoh et al., 2017; Grijzenhout et al., 2016).

In support to this "Hox clock activation timing" hypothesis, precocious transcription of the *Hox* gene clusters has been recently observed upon *in vitro* differentiation of *Smchd1* null mESCs, whose maternal absence *in vivo* produces posterior transformation of the spine, analogous to the ones reported here, both in zebrafish and mice (Benetti et al., 2022; Xue et al., 2022). Beyond the exact mechanism of action, our data are in line with a role for EPOP and Polycomb in the maternal epigenetic priming of *Hox* genes for subsequent silencing in post-implantation embryos, as suggested previously (Benetti et al., 2022).

Overall, our work provides a mechanistic framework for the role of PRC2 in the developmental regulation of mouse antero-posterior body patterning and identifies EPOP as a major player in this process.

Table 1
Summary of the homeotic transformations observed upon *Epop* depletion.

	No. of mice (%)						
	Epop +/+	Epop −/−			Epop +/−		
		del13	del14	Total	Epop$^{mat\Delta}$	Epop$^{pat\Delta}$	Total
Transformation	**(n = 24)**	**(n = 4)**	**(n = 16)**	**(n = 20)**	**(n = 12)**	**(n = 10)**	**(n = 22)**
C2 without spinous process, or fused to C1 (C1→C2)	2 (8.3)	2 (50)	12 (75)	14 (70)	3 (25)	1 (10)	4 (18.2)
Ectopic rib in C7 (C7→T1)	4 (16.7)	3 (75)	15 (93.8)	18 (90)	6 (50)	0 (0)	6 (27.3)
Prominent spinous process in T1 (T1→T2)	1 (4.2)	3 (75)	15 (93.8)	18 (90)	6 (50)	2 (20)	8 (36.4)
T13 is lost (T13→L1)	0 (0)	3 (75)	13 (81.3)	16 (80)	2 (16.7)	1 (10)	3 (13.6)
Six lumbar vertebrae	6 (25)	4 (100)	13 (81.3)	17 (85)	5 (41.7)	8 (80)	13 (59.1)

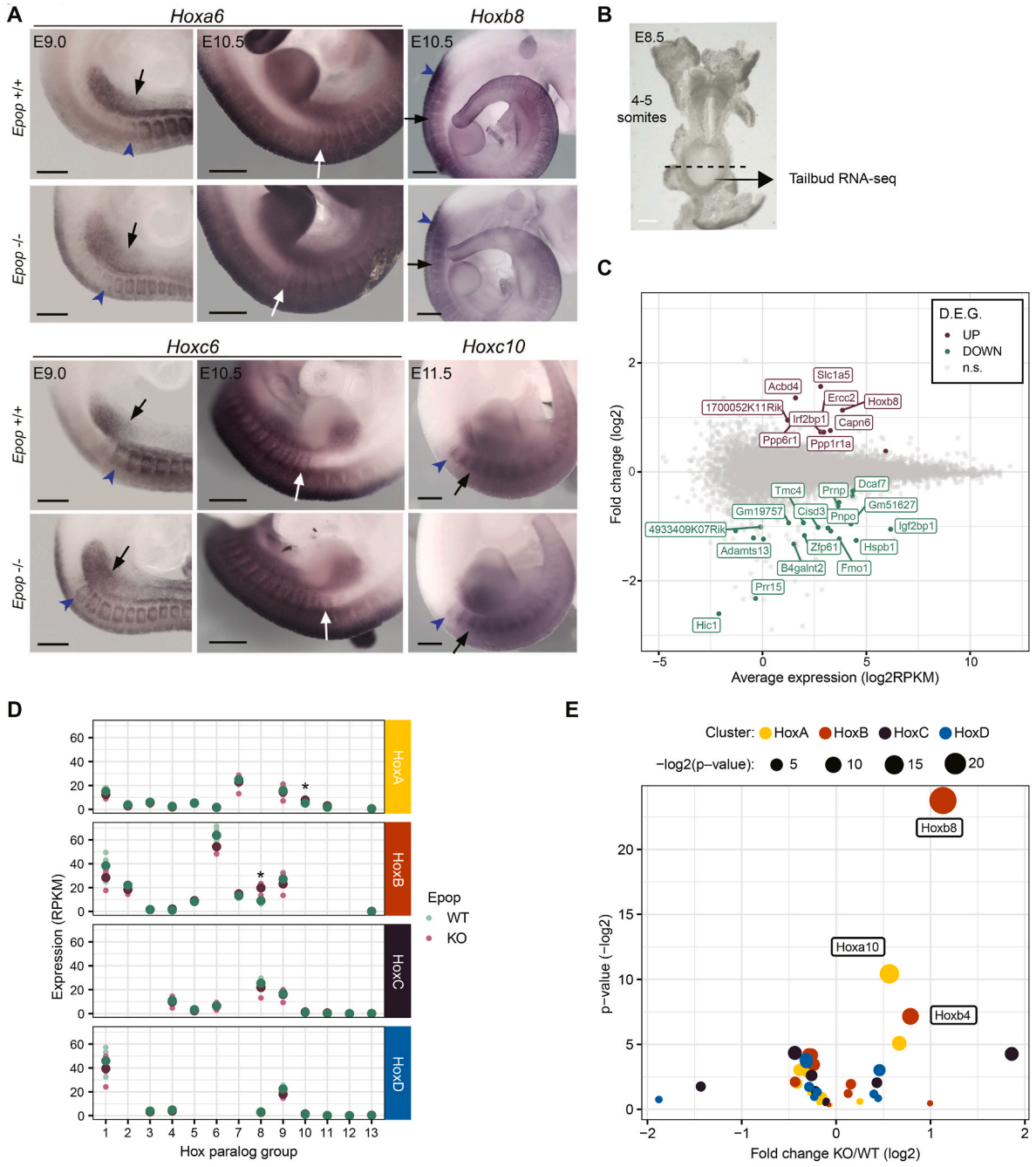

Fig. 4. *Hox* gene misexpression in *Epop* KO embryos. (A) Whole-mount *in situ* hybridization of mouse embryos at E9.0 (left column; scale bar 0.1 mm), E10.5, or E11.5 (middle and right columns, respectively; scale bar 0.5 mm). The black arrows indicate the reference point of a position in the forelimb field in embryos stained with *Hoxa6*, or of the somite located at the anterior border of the limb bud (forelimb in embryos stained for *Hoxb8*, and hindlimb in embryos stained for *Hoxc10*). Blue arrowheads indicate the position of the most anterior somite, with an equivalent level of staining between the wild-type and the *Epop* KO embryos. White arrows indicate the most anterior somite with staining. **(B)** Brightfield of an E8.5 embryo at 4–5 somites before tail dissection. Scale bar, 0.5 mm. **(C)** Expression of *Hox* genes in E8.5 wild-type (green) or *Epop* KO (purple) embryos. Small dots represent individual replicates (four per condition, two female and two male wild-type, and four male KO embryos), and larger dots represent the average of these. *p-value <0.01. **(D)** MA plot of global gene expression changes in E8.5 tailbud of *Epop* KO embryos as compared to wild-type counterparts. Differentially expressed genes are highlighted. **(E)** Volcano plot showing *Hox* gene expression changes in *Epop* KO embryos as compared to WT embryos. (For interpretation of the references to color in this figure legend, the reader is referred to the Web version of this article.)

4. Materials and methods

4.1. Mice

Mouse care and procedures were conducted according to the protocols approved by the PRBB Ethical Committee and by the *Departament de Medi Ambient i Habitatge* of the *Generalitat de Catalunya*.

Hybrid B6CBAF1 (C57Bl/6xCBA/J) mice, 6- to 12-weeks old, were used as embryo donors. Outbred CD1 females mated with vasectomized CD1 males were used as recipient and foster mothers. Transgenic lines were maintained on a C57BL/6J background (background and off-target cleaning for 5 to 6 generations). All animals were purchased from Charles River (L'Arbresle, France).

4.2. Zygote collection

B6CBAF1 females were induced to superovulate by intraperitoneal injection of 5 IU of pregnant mare serum gonadotropin (Intervet, Barcelona, Spain) followed 48 h later by 5 IU of human chorionic gonadotropin (hCG; Farma-Lepori, Barcelona, Spain). Zygotes were collected from the oviducts 22 h after hCG administration in M2, and treated with 150 U/ml hyaluronidase in M2 at 37 °C until dispersion of cumulus cells. Denuded zygotes were then washed and kept in drops of KSOM culture medium (Evolve ZEKS-050) covered with mineral oil (Sigma M8410) at 37 °C under 5 % CO_2.

4.3. Embryo microinjection and in vitro culture

For the knockdown experiment, one-cell embryos at the pronuclear stage were cytoplasmically microinjected with either control siRNA (MISSION® siRNA Universal Negative Control #1 SIC001; Merck) or specific siRNAs targeting the *Epop* transcript (Epop-KD1, 5′-GAGCAUCGAUUCUGAAAUUdTdT-3′; Epop-KD2, 5′-GCUCGAAACUUUGGUGUUAdTdT-3′) at 30 μM in injection buffer (10 mM Tris, 0.1 mM EDTA, pH 7.2). Injected embryos were cultured in KSOM drops (Evolve ZEKS-050) covered with mineral oil (Sigma M8410) until blastocyst stage for qPCR analysis or differential staining. For the knockout experiment, one-cell embryos at the pronuclear stage were microinjected with a sgRNA (Epop-KO1, 5′-ACGCCCCTGAAGCCGCGTCG-3′ Epop-KO2, 5′-AACATCGCCCCCCGTCGACG-3′; Epop-KO3, 5′-AAAGTTTCGAGCGGCGGATC-3′) at 50 ng/μl, and Cas9 at 100 ng/μl (CP01; PNA Bio Inc) in injection buffer (10 mM Tris, 0.1 mM EDTA, pH 7.2), following standard pronuclear injection procedures, whereby microinjection is assessed by around 50 % pronuclear swelling (=2 pl). Injected embryos were then cultured in KSOM drops (ZEKS-050; Evolve) and covered with mineral oil (M8410 Sigma) either until two-cell stage for embryo transfer or until blastocyst stage for mutation analysis.

4.4. Embryo transfer

CD1 female mice were mated with vasectomized males of the same strain, and those with a vaginal plug were used as recipients at 0.5 day postcoitum. Between eight and ten two-cell embryos were dorsally transferred into each oviduct. Pups were naturally delivered 20 days after embryo transfer.

4.5. Blastocyst differential staining and cell counting

Differential staining of blastocysts was performed as previously described (Beringer et al., 2016) using antibodies for EPOP (1:200) (C17orf96 antibody, 61753; Active Motif), NANOG (1:100) (14–5761; Thermo Fisher Scientific), GATA4 (1:100) (sc1237; Santa Cruz Biotechnology) and H3K27me3 (1:500) (ABE044; Merck). After fixation and staining, differential cell counting and scoring of the presence of the H3K27me3 spot from the inactive X chromosome were performed in a genotype-blind fashion. Samples were examined with a Zeiss Cell Observer microscope fitted with an image capture system (for knockdown blastocysts) or a Leica TCS SPE microscope (for KO blastocysts). Fiji software (Image J 1.45q, Wayne Rasband, National Institutes of Health, Bethesda, USA) was used for cell counting. Blastocysts were processed for *Epop* genotyping after imaging.

5. RT-qPCR

Three blastocysts per condition were directly placed into 75 μl of RLT lysis buffer. RNA isolation was performed according to the RNeasy Micro Kit (Qiagen 74004, protocol for tissues) and eluted in 14 μl of water. cDNA was generated from 10 μl of RNA following the qScript cDNA Synthesis Kit (Quantabio) instructions, using 0.75 μl of RT enzyme and 4 μl of 5 × buffer in a total volume of 20 μl. Real-time PCR reactions were performed using SYBR Green I PCR Master Mix (4367659; ThermoFisher Scientific) and the ViiA 7 Real-Time PCR System (ThermoFisher Scientific). The primer sequences were 5′-CTTTCACCTATTAAGGTGCTTGC-3′ and 5′-TGGCATCGGTTCATCATGGTAC-3′ for *Nanog*, and 5′-CTTGACTGCTTCCCCTGTCC-3′ and 5′-GTCCTCCCATCTGCCACTTC-3′ for *Epop*.

5.1. Lysate preparation and genotyping

To genotype blastocysts, each individual embryo was incubated at 55 °C for 1 h in 5 μl of lysis buffer (50 mM KCl, 10 mM Tris pH 8, 0.1 mg/ml gelatin, 0.45 % NP40, 0.45 % Tween 20, 200 μg/ml proteinase K) and covered with 1 μl of oil. Proteinase K was then inactivated at 100 °C for 10 min. The resulting lysate was used as a PCR template with DreamTaq PCR Master Mix (K1082; ThermoFisher Scientific) according to the manufacturer's instructions. To genotype mice, earsnips were collected and digested at 55 °C in 100–500 ml lysis buffer (100 mM Tris-HCl pH 8–8.5, 5 mM EDTA, 0.1 % SDS, 200 mM NaCl, 250–1000 μg/ml proteinase K) for 3 h–20 h. DNA was precipitated with isopropanol and used as a PCR template with Promega PCR Master Mix, according to the manufacturer's instructions. All primers used for genotyping are listed in Table S1.

5.2. Mutation analysis

To analyze the indels generated after CRISPR/CAS9 injection, the coding sequence of *Epop* was amplified by PCR using labeled primers (Table S1). The PCR product was then used for conventional 2 % agarose gel electrophoresis and fragment-size analysis by capillary electrophoresis for single-base resolution (by Life Technologies, service available from Universitat Pompeu Fabra, Barcelona). The *Epop* del14 and del13 alleles were also sequenced (Sanger sequencing service, Eurofins) to confirm the presence of the mutations.

5.3. Western blot

Placentas and heads from E12.5 embryos from a cross between two *Epop* +/− mice or an *Epop* −/− female and an *Epop* +/− male were collected in PBS and directly frozen at −80 °C. Tissue was resuspended in a lysis buffer (1 % SDS, 1 mM EDTA, 1 mM EGTA, 15 mM Tris HCl pH 7.4) supplemented with phosphatase and protease inhibitors and homogenized using the TissueRuptor II (Qiagen). Protein lysates were then boiled at 95 °C for 10 min and sonicated on a Bioruptor for 5 min (30 s ON, 30 s OFF) or until the lysate was clear. Additional debris was removed by centrifugation at 16,000 *g* for 10 min. Protein extracts were quantified using BCA, and 20 μg of each sample was used for SDS-PAGE. The presence of EPOP (Active Motif, 61753), SUZ12 (Cell Signaling, 37375), and H3K27me3 (Merck, 07–449) was assessed by Western blot.

5.4. Histopathological analysis

Four wild-type and four KO (*Epop* del14) mice, 13- to 16-weeks old (two males and two females of each genotype), and two pregnant females at E12.5 from a heterozygous cross (*Epop* wt/del13), were used. Mice were euthanized by lethal exposure to CO_2, and lung, large intestine, liver, spleen, small and large intestines, stomach, heart, kidney, pancreas, skeletal muscle, skin, bone, bone marrow, brain, testes, epididymis, uterus, ovaries, vagina, and placenta samples were collected and fixed in 4 % buffered formalin for 24 h, except for testis, which was fixed using Bouin's solution. The bone tissue was decalcified for 14 days using OSTEOSOFT ® (1017281000, VWR). Afterwards, samples were washed in PBS and processed using a series of graded alcohol and xylene, followed by paraffin embedding. Tissue sections of 3–4 μm thickness were cut using rotary microtome, affixed on glass slides, and stained with a hematoxylin and eosin routine protocol. Placentas were stained with periodic acid–Schiff (PAS) to better highlight and

differentiate the placental zones. Macroscopical and microscopical studies were done in a blinded fashion.

5.5. Skeletal stainings

Skeletal whole mounts were performed as previously described (Vizán et al., 2020). Briefly, the completely eviscerated and skinned animals were fixed in 96 % ethanol for five days and transferred to acetone for two days. Staining was performed with 0.005 % Alizarin Red S, 0.015 % Alcian blue 8 GS in 5 % acetic acid, 5 % H_2O, and 90 % ethanol for 5 days at room temperature. Samples were washed in H_2O and cleared for two days in 1 % KOH, followed by three clearing steps, in 0.8 % KOH and 20 % glycerol, in 0.5 % KOH and 50 % glycerol, and in 0.2 % KOH and 80 % glycerol, for one week each. Cleared skeletons were stored in 100 % glycerol.

5.6. Micro-computed tomography (Micro-CT)

Full body 3D tomographic images were acquired using an X-ray micro-CT (SkyScan1278, Bruker) using the following parameters: Al 0.5 mm filter, 50 kVp X-ray source voltage, 300 μA current, 110 ms camera exposure time per projection, 360° scan with 0.8 rotation step. The tomographic three-dimensional (3D) images obtained had a total of 450 slices with isotropic 51 μm pixel size and a resolution of 1024 × 1024 pixels per slice. Three-dimensional (3D) images were automatically reconstructed using the NRecon version 2.2.0.6 (Bruker) (Minimum for CS to Image Conversion = 0.0; Maximum for CS to Image Conversion = 0.04; Beam Hardening Correction = 20 %) and preclinical analysis performed in CTVox software (Bruker).

5.7. Whole-mount in situ hybridization

Whole-mount *in situ* hybridization was performed using antisense digoxigenin-labeled probes for *Hoxa6* (IMAGE, clone #8733856, containing the entire open reading frame), *Hoxc6* (1140 bp cDNA fragment containing the homeobox and the entire 3′ UTR), *Hoxb8* (550 bp cDNA fragment containing the homeobox and part of the 3′ UTR) and *Hoxc10* (1091 bp cDNA fragment containing the entire open reading frame). The probes were prepared by *in vitro* transcription from linearized plasmids containing the Hox cDNA fragment using the DIG RNA labeling Mix (11277073910; Roche). After transcription, the DNA template was removed with DNase I treatment, and the probes were precipitated with ethanol and resuspended in 100 μl of TE pH 8.0. Embryos were collected at E9.5, E10.5, and E11.5 in PBS and fixed in 4 % paraformaldehyde in PBS (PFA) at 4 °C overnight, washed in PBT (PBS containing 0.1 % Tween 20), and sequentially dehydrated with methanol through a series of 25 %, 50 %, 75 %, and 100 % methanol in PBT washes. Embryos were then rehydrated through a reverse methanol/PBT series and washed extensively in PBT at room temperature. Embryos were bleached in 6 % H_2O_2 in PBT for 1 h at room temperature, washed with PBT, and treated with 10 μg/ml proteinase K at room temperature for 6, 9 or 12 min for the E9.5, E10.5, or E11.5 embryos, respectively. Proteinase K activity was stopped by incubation in glycine at 2 mg/ml in PBT for 10 min at room temperature. Embryos were then washed in PBT at room temperature, post-fixed in 4 % PFA, 0.2 % glutaraldehyde at 4 °C for 20 min, washed three times in PBT, and equilibrated in hybridization solution of 50 % formamide, 1.3 × SSC pH 5.5 (whereby 20 × SSC is 3 M NaCl, 300 mM sodium citrate), 5 mM EDTA, 0.2 % Tween 20, 0.5 % CHAPS, 50 μg/ml yeast tRNA (R5636; Sigma), 100 μg/ml heparin (H3149; Sigma) at 65 °C for 1 h. Embryos were then incubated in hybridization solution containing the DIG-labeled antisense probes (6 μl of the stock solution/ml) overnight at 65 °C. Embryos were washed twice in wash solution, 30 min each at 65 °C, then in a 1:1 solution of wash solution and TBST (140 mM NaCl, 2.7 mM KCl, 25 mM Tris HCl, pH 8.0, 0.1 % Tween 20) for additional 30 min at 65 °C, and finally washed three times in TBST at room temperature. Embryos were then washed in MABT (100 mM maleic acid, 150 mM NaCl, 0.1 % Tween-20, pH 7.5) at room temperature and incubated in blocking solution (MABT containing 1 % blocking reagent; #11096176001; Roche) containing 10 % sheep serum for 3 h at room temperature. Embryos were incubated overnight at 4 °C in blocking solution containing 1 % sheep serum and a 1:2000 dilution of AP-conjugated anti-DIG antibody (11093274910; Roche). Embryos were then washed extensively for 24 h in MABT at room temperature, then equilibrated in NTMT (100 mM Tris HCl, pH 9.5, 50 mM $MgCl_2$, 100 mM NaCl, 0.1 % Tween 20), and developed with NBT/BCIP (1:50 dilution of the stock) (11681451001; Roche) in NTMT at room temperature in the dark. The developing reaction was stopped with PBT, and embryos were fixed in 4 % PFA for 6 h and then stored in PBT.

5.8. RNA-seq

E8.5 embryos were collected and dissected in PBS. The second half of the tailbud, including the presomitic mesoderm, was placed in 350 μl of RLT buffer with B-mercaptoethanol (RNeasy Micro kit; Qiagen) and stored at −80 °C. RNA extraction was performed according to the manufacturer's instructions.

cDNA was generated using Smart-seq2 protocol (Picelli et al., 2014). Briefly, total RNA was reverse transcribed using betaine and increasing the magnesium chloride concentration, template switching was performed using a locked nucleic acid (LNA) and elimination of purification step before preamplification PCR to obtain an increased cDNA yield from single cells. cDNA was measured with Qubit dsDNA High Sensitivity assay (Q32851, Invitrogen) to determine the concentration and was analyzed using Agilent Bioanalyzer or Fragment analyzer High Sensitivity assay (5067-4626 or DNF-474, Agilent) to check size distribution profile. Then, from this cDNA, libraries were prepared using NEBNext® Ultra DNA Library Prep for Illumina® kit (E7370) according to the manufacturer's protocol. Briefly, 5 ng of cDNA were fragmented at a range size of 200–500 bp using Covaris S2, then were subjected to end repair and addition of "A" bases to 3′ ends, ligation of adapters and USER excision. All purification steps were performed using AgenCourt AMPure XP beads (A63882, Beckman Coulter). Library amplification was performed by PCR using NEBNext® Multiplex Oligos for Illumina® (96 Unique Dual Index Primer Pairs, E6440). Final libraries were analyzed using Agilent Bioanalyzer or Fragment analyzer High Sensitivity assay to estimate the quantity and check size distribution and were then quantified by qPCR using the KAPA Library Quantification Kit (KK4835, KapaBiosystems). Libraries were sequenced 2 * 50 + 8 +8 bp on Illumina's NextSeq2000.

The RNA-seq samples were mapped against the mm10 mouse genome assembly using TopHat (Trapnell et al., 2009), using the option –g 1 to discard those reads that could not be uniquely mapped to just one region. DESeq2 (Love et al., 2014) was run to quantify the expression of every annotated transcript using the RefSeq (O'Leary et al., 2016) catalog of exons and to identify each set of differentially expressed genes. Raw data and processed information of the RNA-seq experiments generated in this article have been deposited in the National Center for Biotechnology Information Gene Expression Omnibus (NCBI GEO) (Barrett et al., 2013) repository under the accession number GSE255167.

CRediT authorship contribution statement

Ivano Mocavini: Writing – review & editing, Writing – original draft, Investigation, Formal analysis, Conceptualization. **Anna Mallol:** Writing – original draft, Investigation, Formal analysis, Conceptualization. **Arantxa Gutierrez:** Investigation. **Paul Chammas:** Investigation, Conceptualization. **Ana Carretero:** Investigation. **André Dias:** Investigation. **Enrique Blanco:** Writing – review & editing, Formal analysis, Data curation. **Irene Rodriguez Arce:** Writing – review & editing, Investigation. **Moises Mallo:** Writing – review & editing, Investigation, Funding acquisition, Conceptualization. **Luciano Di Croce:**

Supervision, Funding acquisition, Conceptualization. **Bernhard Payer:** Writing – review & editing, Supervision, Funding acquisition, Conceptualization.

Acknowledgements

We are grateful to the CRG Core Technologies (the Advanced Light Microscopy Unit; Genomic Unit) and the PRBB animal facility for their support and assistance in this work. We thank Veronica A. Raker for scientific editing of the manuscript.

The Di Croce laboratory is supported by the Spanish Ministry of Economy, Industry and Competitiveness (MEIC) (PID2022-142679NB-I00 and 'Planes complementarios' STOP-DMG N6958), "Fundación Vencer El Cancer" (VEC), the European Regional Development Fund (FEDER), "laCaixa" Foundation (CI24-10473), and from AGAUR (2023 LLAV 00093). Payer laboratory was supported by Agencia Estatal de Investigación (AEI) of the Spanish Grant PID2021-123383NB-I00 funded by MCIN/AEI/10.13039/501100011033/FEDER, UE and the Agencia de Gestió d'Ajuts Universitaris i de Recerca (AGAUR) 2021 grant SGR 01222. We thank Xojo Inc. for providing the software platform that enabled our custom tool for archiving, organizing, and extracting data from scientific publications.

Ivano Mocavini was supported by an FPI fellowship (BES-2017-081035). We acknowledge support of the Spanish Ministry of Science and Innovation through the Centro de Excelencia Severo Ochoa (CEX2020-001049-S, MCIN/AEI/10.13039/501100011033), and the Generalitat de Catalunya through the CERCA programme.

Appendix A. Supplementary data

Supplementary data related to this article can be found at https://doi.org/10.1016/j.ydbio.2025.08.014.

Data availability

RNA-seq data is deposited in GEO with accession number GSE255167.

References

Akasaka, T., Kanno, M., Balling, R., Mieza, M.A., Taniguchi, M., Koseki, H., 1996. A role for mel-18, a Polycomb group-related vertebrate gene, during the anteroposterior specification of the axial skeleton. Development 122, 1513–1522.

Akasaka, T., van Lohuizen, M., van der Lugt, N., Mizutani-Koseki, Y., Kanno, M., Taniguchi, M., Vidal, M., Alkema, M., Berns, A., Koseki, H., 2001. Mice doubly deficient for the Polycomb group genes Mel18 and Bmi1 reveal synergy and requirement for maintenance but not initiation of Hox gene expression. Development 128, 1587–1597.

Arecco, N., Mocavini, I., Blanco, E., Ballaré, C., Libman, E., Bonnal, S., Irimia, M., Di Croce, L., 2024. Alternative splicing decouples local from global PRC2 activity. Mol. Cell 84, 1049–1061.e8.

Barrett, T., Wilhite, S.E., Ledoux, P., Evangelista, C., Kim, I.F., Tomashevsky, M., Marshall, K.A., Phillippy, K.H., Sherman, P.M., Holko, M., et al., 2013. NCBI GEO: archive for functional genomics data sets–update. Nucleic Acids Res. 41, D991–D995.

Baskind, H.A., Na, L., Ma, Q., Patel, M.P., Geenen, D.L., Wang, Q.T., 2009. Functional conservation of Asxl2, a murine homolog for the Drosophila enhancer of trithorax and polycomb group gene Asx. PLoS One 4, e4750.

Bel, S., Coré, N., Djabali, M., Kieboom, K., Van der Lugt, N., Alkema, M.J., Van Lohuizen, M., 1998. Genetic interactions and dosage effects of Polycomb group genes in mice. Development 125, 3543–3551.

Benetti, N., Gouil, Q., Tapia Del Fierro, A., Beck, T., Breslin, K., Keniry, A., McGlinn, E., Blewitt, M.E., 2022. Maternal SMCHD1 regulates Hox gene expression and patterning in the mouse embryo. Nat. Commun. 2021, 459528.

Beringer, M., Pisano, P., Di Carlo, V., Blanco, E., Chammas, P., Vizán, P., Gutiérrez, A., Aranda, S., Payer, B., Wierer, M., et al., 2016. EPOP functionally links elongin and polycomb in pluripotent stem cells. Mol. Cell 64, 645–658.

Carapuço, M., Nóvoa, A., Bobola, N., Mallo, M., 2005. Hox genes specify vertebral types in the presomitic mesoderm. Genes Dev. 19, 2116–2121.

Chammas, P., Mocavini, I., Di Croce, L., 2019. Engaging chromatin: PRC2 structure meets function. Br. J. Cancer 122, 315–328.

Condemi, L., Mocavini, I., Aranda, S., Di Croce, L., 2025. Polycomb function in early mouse development. Cell Death Differ. 32, 90–99.

del Mar Lorente, M., Marcos-Gutiérrez, C., Pérez, C., Schoorlemmer, J., Ramírez, A., Magin, T., Vidal, M., 2000. Loss- and gain-of-function mutations show a polycomb group function for Ring1A in mice. Development 127, 5093–5100.

Deschamps, J., Duboule, D., 2017. Embryonic timing, axial stem cells, chromatin dynamics, and the Hox clock. Genes Dev. 31, 1406–1416.

Deschamps, J., van Nes, J., 2005. Developmental regulation of the Hox genes during axial morphogenesis in the mouse. Development 132, 2931–2942.

Endoh, M., Endo, T.A., Shinga, J., Hayashi, K., Farcas, A., Ma, K.-W., Ito, S., Sharif, J., Endoh, T., Onaga, N., et al., 2017. PCGF6-PRC1 suppresses premature differentiation of mouse embryonic stem cells by regulating germ cell-related genes. eLife 6.

Fisher, C.L., Lee, I., Bloyer, S., Bozza, S., Chevalier, J., Dahl, A., Bodner, C., Helgason, C. D., Hess, J.L., Humphries, R.K., et al., 2010. Additional sex combs-like 1 belongs to the enhancer of trithorax and polycomb group and genetically interacts with Cbx2 in mice. Dev. Biol. 337, 9–15.

Gentile, C., Kmita, M., 2020. Polycomb repressive complexes in Hox gene regulation: silencing and beyond: the functional dynamics of polycomb repressive complexes in Hox gene regulation. Bioessays 42, e1900249.

Grijzenhout, A., Godwin, J., Koseki, H., Gdula, M.R., Szumska, D., McGouran, J.F., Bhattacharya, S., Kessler, B.M., Brockdorff, N., Cooper, S., 2016. Functional analysis of AEBP2, a PRC2 Polycomb protein, reveals a Trithorax phenotype in embryonic development and in ESCs. Development 143, 2716–2723.

Horan, G.S., Ramírez-Solis, R., Featherstone, M.S., Wolgemuth, D.J., Bradley, A., Behringer, R.R., 1995. Compound mutants for the paralogous hoxa-4, hoxb-4, and hoxd-4 genes show more complete homeotic transformations and a dose-dependent increase in the number of vertebrae transformed. Genes Dev. 9, 1667–1677.

Inoue, A., 2023. Noncanonical imprinting: intergenerational epigenetic inheritance mediated by Polycomb complexes. Curr. Opin. Genet. Dev. 78, 102015.

Isono, K.-I., Fujimura, Y.-I., Shinga, J., Yamaki, M., O-Wang, J., Takihara, Y., Murahashi, Y., Takada, Y., Mizutani-Koseki, Y., Koseki, H., 2005. Mammalian polyhomeotic homologues Phc2 and Phc1 act in synergy to mediate polycomb repression of Hox genes. Mol. Cell Biol. 25, 6694–6706.

Kim, J.J., Kingston, R.E., 2022. Context-specific Polycomb mechanisms in development. Nat. Rev. Genet. 23, 680–695.

Lau, M.S., Schwartz, M.G., Kundu, S., Savol, A.J., Wang, P.I., Marr, S.K., Grau, D.J., Schorderet, P., Sadreyev, R.I., Tabin, C.J., et al., 2017. Mutation of a nucleosome compaction region disrupts Polycomb-mediated axial patterning. Science 355, 1081–1084.

Li, X., Isono, K.-I., Yamada, D., Endo, T.A., Endoh, M., Shinga, J., Mizutani-Koseki, Y., Otte, A.P., Casanova, M., Kitamura, H., et al., 2011. Mammalian polycomb-like Pcl2/Mtf2 is a novel regulatory component of PRC2 that can differentially modulate polycomb activity both at the Hox gene cluster and at Cdkn2a genes. Mol. Cell Biol. 31, 351–364.

Liefke, R., Karwacki-Neisius, V., Shi, Y., 2016. EPOP interacts with elongin BC and USP7 to modulate the chromatin landscape. Mol. Cell 64, 659–672.

Loda, A., Collombet, S., Heard, E., 2022. Gene regulation in time and space during X-chromosome inactivation. Nat. Rev. Mol. Cell Biol. 23, 231–249.

Love, M.I., Huber, W., Anders, S., 2014. Moderated estimation of fold change and dispersion for RNA-seq data with DESeq2. Genome Biol. 15, 550.

Mak, W., Nesterova, T.B., de Napoles, M., Appanah, R., Yamanaka, S., Otte, A.P., Brockdorff, N., 2004. Reactivation of the paternal X chromosome in early mouse embryos. Science 303, 666–669.

Mallo, M., Wellik, D.M., Deschamps, J., 2010. Hox genes and regional patterning of the vertebrate body plan. Dev. Biol. 344, 7–15.

McIntyre, D.C., Rakshit, S., Yallowitz, A.R., Loken, L., Jeannotte, L., Capecchi, M.R., Wellik, D.M., 2007. Hox patterning of the vertebrate rib cage. Development 134, 2981–2989.

Mohammed, H., Hernando-Herraez, I., Savino, A., Scialdone, A., Macaulay, I., Mulas, C., Chandra, T., Voet, T., Dean, W., Nichols, J., et al., 2017. Single-cell landscape of transcriptional heterogeneity and cell fate decisions during mouse early gastrulation. Cell Rep. 20, 1215–1228.

Neijts, R., Amin, S., van Rooijen, C., Tan, S., Creyghton, M.P., de Laat, W., Deschamps, J., 2016. Polarized regulatory landscape and Wnt responsiveness underlie Hox activation in embryos. Genes Dev. 30, 1937–1942.

O'Leary, N.A., Wright, M.W., Brister, J.R., Ciufo, S., Haddad, D., McVeigh, R., Rajput, B., Robbertse, B., Smith-White, B., Ako-Adjei, D., et al., 2016. Reference sequence (RefSeq) database at NCBI: current status, taxonomic expansion, and functional annotation. Nucleic Acids Res. 44, D733–D745.

Picelli, S., Faridani, O.R., Björklund, A.K., Winberg, G., Sagasser, S., Sandberg, R., 2014. Full-length RNA-seq from single cells using Smart-seq2. Nat. Protoc. 9, 171–181.

Pijuan-Sala, B., Griffiths, J.A., Guibentif, C., Hiscock, T.W., Jawaid, W., Calero-Nieto, F. J., Mulas, C., Ibarra-Soria, X., Tyser, R.C.V., Ho, D.L.L., et al., 2019. A single-cell molecular map of mouse gastrulation and early organogenesis. Nature 566, 490–495.

Rothberg, J.L.M., Maganti, H.B., Jrade, H., Porter, C.J., Palidwor, G.A., Cafariello, C., Battaion, H.L., Khan, S.T., Perkins, T.J., Paulson, R.F., et al., 2018. Mtf2-PRC2 control of canonical Wnt signaling is required for definitive erythropoiesis. Cell Discov. 4, 21.

Schuettengruber, B., Bourbon, H.-M., Di Croce, L., Cavalli, G., 2017. Genome regulation by polycomb and Trithorax: 70 years and counting. Cell 171, 34–57.

Soshnikova, N., Duboule, D., 2009. Epigenetic temporal control of mouse Hox genes in vivo. Science 324, 1320–1323.

Suzuki, M., Mizutani-Koseki, Y., Fujimura, Y.-I., Miyagishima, H., Kaneko, T., Takada, Y., Akasaka, T., Tanzawa, H., Takihara, Y., Nakano, M., et al., 2002. Involvement of the Polycomb-group gene Ring1B in the specification of the anterior-posterior axis in mice. Development 129, 4171–4183.

Takeuchi, T., Yamazaki, Y., Katoh-Fukui, Y., Tsuchiya, R., Kondo, S., Motoyama, J., Higashinakagawa, T., 1995. Gene trap capture of a novel mouse gene, jumonji, required for neural tube formation. Genes Dev. 9, 1211–1222.
Takeuchi, T., Kojima, M., Nakajima, K., Kondo, S., 1999. Jumonji gene is essential for the neurulation and cardiac development of mouse embryos with a C3H/He background. Mech. Dev. 86, 29–38.
Takihara, Y., Tomotsune, D., Shirai, M., Katoh-Fukui, Y., Nishii, K., Motaleb, M.A., Nomura, M., Tsuchiya, R., Fujita, Y., Shibata, Y., et al., 1997. Targeted disruption of the mouse homologue of the Drosophila polyhomeotic gene leads to altered anteroposterior patterning and neural crest defects. Development 124, 3673–3682.
Tapial, J., Ha, K.C.H., Sterne-Weiler, T., Gohr, A., Braunschweig, U., Hermoso-Pulido, A., Quesnel-Vallières, M., Permanyer, J., Sodaei, R., Marquez, Y., et al., 2017. An atlas of alternative splicing profiles and functional associations reveals new regulatory programs and genes that simultaneously express multiple major isoforms. Genome Res. 27, 1759–1768.
Trapnell, C., Pachter, L., Salzberg, S.L., 2009. TopHat: discovering splice junctions with RNA-Seq. Bioinformatics 25, 1105–1111.
van der Lugt, N.M., Domen, J., Linders, K., van Roon, M., Robanus-Maandag, E., te Riele, H., van der Valk, M., Deschamps, J., Sofroniew, M., van Lohuizen, M., 1994. Posterior transformation, neurological abnormalities, and severe hematopoietic defects in mice with a targeted deletion of the bmi-1 proto-oncogene. Genes Dev. 8, 757–769.
Vizán, P., Gutiérrez, A., Espejo, I., García-Montolio, M., Lange, M., Carretero, A., Lafzi, A., de Andrés-Aguayo, L., Blanco, E., Thambyrajah, R., et al., 2020. The Polycomb-associated factor PHF19 controls hematopoietic stem cell state and differentiation. Sci. Adv. 6, eabb2745.
Wang, J., Mager, J., Schnedier, E., Magnuson, T., 2002. The mouse PcG gene eed is required for Hox gene repression and extraembryonic development. Mamm. Genome 13, 493–503.
Wang, S., He, F., Xiong, W., Gu, S., Liu, H., Zhang, T., Yu, X., Chen, Y., 2007. Polycomblike-2-deficient mice exhibit normal left-right asymmetry. Dev. Dyn. 236, 853–861.
Wellik, D.M., Capecchi, M.R., 2003. Hox10 and Hox11 genes are required to globally pattern the mammalian skeleton. Science 301, 363–367.
Xue, S., Ly, T.T.N., Vijayakar, R.S., Chen, J., Ng, J., Mathuru, A.S., Magdinier, F., Reversade, B., 2022. HOX epimutations driven by maternal SMCHD1/LRIF1 haploinsufficiency trigger homeotic transformations in genetically wildtype offspring. Nat. Commun. 13, 1–11.
Yu, B.D., Hess, J.L., Horning, S.E., Brown, G.A., Korsmeyer, S.J., 1995. Altered Hox expression and segmental identity in Mll-mutant mice. Nature 378, 505–508.